Journal of Power Sources 688 (2026) 240447

Contents lists available at ScienceDirect

Journal of Power Sources

journal homepage: www.elsevier.com/locate/jpowsour

Deep learning-enhanced physical modelling for tape-casting slurry microstructures of solid oxide cell substrates

Tan Le-Dinh [a,b,c], Utkarsh Vijay [a,d], Diego E. Galvez-Aranda [a], Hartmut Schlenz [c], Norbert H. Menzler [c], Olivier Guillon [c], Alejandro A. Franco [a,b,d,e,*]

[a] Laboratoire de Réactivite et de Chimie des Solides, UMR CNRS 7314, Université de Picardie Jules Verne, 80039 Amiens Cedex, France
[b] Réseau sur le Stockage Electrochimique de l'Energie (RS2E), Hub de l'Energie, FR CNRS 3459, 15 rue Baudelocque, 80039, Amiens, France
[c] Forschungszentrum Jülich GmbH, Institute of Energy Materials and Devices (IMD), IMD-2: Materials Synthesis and Processing, 52428, Jülich, Germany
[d] ALISTORE-European Research Institute, Hub de l'Energie, FR CNRS 3104, 15 rue Baudelocque, 80039 Amiens Cedex, France
[e] Institut Universitaire de France, 1 rue Descartes, 75231 Paris Cedex 05, France

HIGHLIGHTS

- A hybrid surrogate workflow for supporting manufacturing slurries.
- Deep learning to predict 3D slurry microstructures of the fuel-electrode support.
- A digital modelling tool to accelerate the slurry simulation.

ARTICLE INFO

Keywords:
Solid oxide cells
Anode substrate
Tape casting
Computational modelling
Discrete element method
Deep learning

ABSTRACT

Efficient modelling of tape-cast slurry microstructures is a key requirement for accelerating the manufacturing development of solid oxide cell (SOC) fuel-electrode substrates. While physics-based discrete element method (DEM) simulations provide high-fidelity microstructural insight, their computational cost restricts rapid process exploration. This work presents a hybrid surrogate modelling framework that combines DEM simulations with deep learning to efficiently model tape-cast slurry microstructures of the fuel-electrode substrate. Our proposed framework captures how processing parameters influence the resulting slurry microstructure at the particle scale, enabling prediction of the slurry microstructure without the cost of full-scale DEM simulations. The hybrid model reliably reproduces key microstructural characteristics and microstructural metrics consistent with physics-based observations of DEM-generated data, demonstrating the robustness of the hybrid modelling strategy. Our hybrid surrogate approach minimised the computational cost versus the pure DEM simulation, reducing the calculation time from 1230 to 30 min for the whole slurry simulation process. Although certain slurry microstructures still present minor deviations, the approach reduces reliance on computationally intensive DEM simulations and supports faster validation and early-stage optimisation. As a proof of concept, our work provides a foundation for developing data-efficient and scalable digital modelling tools that could support high-throughput and guide experiments in the SOC manufacturing research field.

1. Introduction

Renewable or green energy sources are becoming more desirable due to the dual challenges of climate change and energy security. Amongst the diverse technologies being advanced to utilise green energy, Solid oxide cells (SOCs) have emerged as a promising solution in the search for cleaner and more efficient energy solutions. There are two operating modes in a unit of SOCs within the high-temperature range from 650 °C to 900 °C [1,2], namely solid oxide fuel cell and solid oxide electrolysis cell. In fuel cell mode, SOCs directly convert the electrochemical energy of the fuel into electrical energy. Alternatively, in SOEC mode, the solid oxide cell technology generates oxygen and hydrogen from water splitting. Owing to the high-temperature operation of SOCs, the fuel flexibility of SOCs, which allows operation on carbohydrate fuels with internal or external reforming, is a notable benefit. SOCs have a much better tolerance against such contaminants and may

* Correspondence to: Laboratoire de Réactivité et Chimie des Solides (LRCS), Université de Picardie Jules Verne, Hub de l'Energie, UMR CNRS 7314, 15 rue Baudelocque, 80039 Amiens, France.
E-mail address: alejandro.franco@u-picardie.fr (A.A. Franco).

https://doi.org/10.1016/j.jpowsour.2026.240447
Received 27 February 2026; Received in revised form 12 May 2026; Accepted 17 May 2026
Available online 13 June 2026

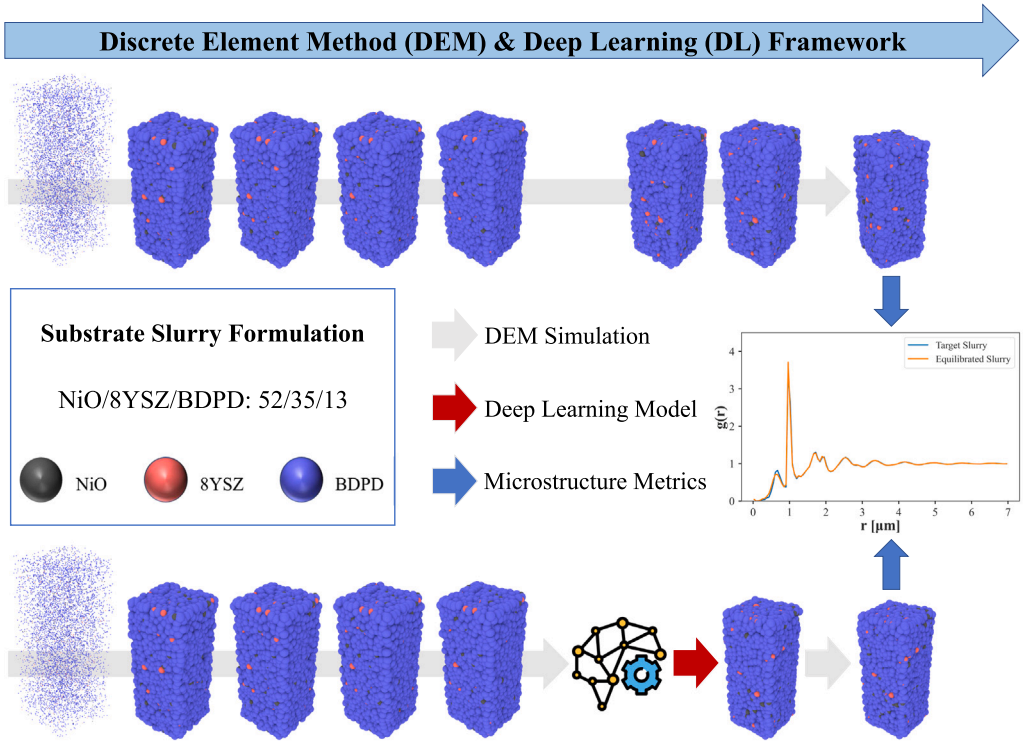

Fig. 1. Schematic representation of the hybrid surrogate model for 3D slurry microstructure prediction of the fuel-electrode substrate. The workflow integrates DEM simulations (grey arrows) and the DL (red arrow) at the slurry preparation stage, where the slurries generated from the full DEM simulation are our ground-truth data. The equilibrated slurry obtained from the hybrid model was compared with the target slurry from the pure DEM simulation.

even use impurities such as CO as fuel. In contrast, low-temperature fuel cells, such as proton exchange membrane fuel cells (PEMFCs), are hypersensitive to the presence of certain fuel gas impurities, particularly CO and CO_2 [2,3]. Nevertheless, one of the main objectives of the research and development of SOCs is to reduce the cost associated with low-cost materials, the commercialisation of cell and stack as well as component manufacturing, and performance improvement [4]. It is, therefore, necessary to implement manufacturing procedures that lower the cost of production for each SOC unit.

A tape-casting process, also called a doctor-blading or knife-coating process, is a well-known technique that is widely used for the manufacture of thin and flat ceramic substrates in the ceramics industry [5,6]. This technology enables the low-cost, large-scale production of ceramic green tapes with a consistent thickness between 5 and 1000 μm in the final fired state [7]. These ceramic green sheets serve as the foundational material for the production of substrates and ceramic multilayer devices, such as gas sensors, actuators, high-integrated circuits, inductors, and capacitors [8]. The secret to the successful implementation of such applications is to guarantee that the green tape has exactly the proper characteristics when it is manufactured, as the green tape ultimately governs the characteristics of the end-sintered tape. In the context of fuel-electrode supported SOCs, tape casting is of particular importance for fabricating the fuel-electrode support/substrate, which not only provides the mechanical backbone for the entire cell but also defines the microstructural template for the subsequent functional layers. As the thickness, porosity, and homogeneity of this support strongly affect the mechanical behaviour and the subsequent coating technologies and layer characteristics, its fabrication requires precise control and optimisation. Nevertheless, ceramic green tape properties are commonly attained by trial and error rather than through systematic initial testing and optimisation [9,10]. It is, therefore, costly for manufacturers due to material and product waste. Meanwhile, the preparation of a good slurry is one of the most important aspects of acquiring the required green tape since the material flow and the rheological behaviour of the slurry establish the ultimate properties as well as the quality of the casting tape [11,12]. Because of this complexity, computational simulation techniques can be an alternative approach to model the slurry of the fuel-electrode substrate.

Building upon the ARTISTIC research initiative [13] for lithium-ion batteries [14–19], the Discrete Element Method (DEM) is applied to mimic the solvent-based slurry phase of the fuel-electrode substrate and its drying as a function of manufacturing parameters (e.g. the solid content, the material particle size distribution). Since the slurry composition of the fuel electrode substrate comprises NiO (Green Nickel Oxide), 8YSZ (8 mol% Yttria-Stabilised Zirconia), solvent, and organic materials [20], our DEM approach simulates the solvent-based slurry by investigating the interplay between three types of particles, namely NiO, 8YSZ, and Binder Dispersant Plasticiser Domain (BDPD) including solvents and organic material. Specifically, this DEM model allows the generation of the solvent-based slurry at the mesoscale by using Force Fields (FFs) to characterise the physicochemical interaction between pairs of material particles in the equilibrated casting slurry. Nonetheless, mesoscale computational simulation of the slurry still requires faster preprocessing processes to save computational cost. The rapid development of high-performance computing and the blooming artificial intelligence field are the keys to accelerating the computational science concerning the SOC manufacturing process as a whole. In this context, machine learning and, more recently, deep learning (DL) techniques have been increasingly employed to complement physics-based simulations, particularly when dealing with high-dimensional and spatially correlated data. Amongst these, Convolutional Neural Networks (CNNs) have emerged as one of the most effective architectures for capturing spatial features, which makes them especially suitable for modelling complex microstructures.

A CNN, also known as a ConvNet, is a type of artificial neural network widely used in traditional computer vision tasks, for instance, video analysis, image classification [21,22], object localisation, object detection [23,24], and image segmentation [25]. Overall, CNNs are

Table 1
Summary of the simulation configuration for data generation.

Parameters per simulation	Slurry simulation	Description
Timestep (μs)	0.0001	Δt to update the positions
Total steps	6 000 000	Total number of iterations
Simulation time (μs)	600	Total duration of the simulation
Frames storage interval	50 000	Steps at which coordinates are recorded
Total number of frames	121	Coordinates are printed at specified frame storage interval
Wall time (hrs.)	20.5	Total DEM simulation time. This depends upon computational resources available.

frequently composed of multiple convolutional layers, certain fully connected layers, and a classification softmax layer that uses, for example, a cross-entropy loss. In addition to classification, CNNs are used to cope with regression problems, which involves using a linear activation function (also known as the "identity function") in the final fully connected regression layer instead of a softmax layer [26]. Furthermore, since the 3D-slurry microstructure is typically similar to a specialised type of grid structure, CNNs are advanced approaches for analysing the slurry microstructure from the DEM model. Consequently, the equilibrated microstructure modelled by DEM is obtained faster after several timesteps rather than running the entire DEM simulation, thereby lowering computational costs.

In this work, we propose a hybrid surrogate model coupling DEM and DL to accelerate the simulation of the slurry phase in the substrate fabrication of fuel-electrode supported SOCs. The workflow is shown in Fig. 1. As proof of concept, we focus on a specific formulation (52% of NiO, 35% of 8YSZ, and 13% of BDPD) with a set of FFs to generate the dataset. The DL model is trained using physics-based data of the slurry microstructure generated from DEM simulation based upon our ARTISTIC framework [27]. Specifically, the CNN model was employed with a slightly altered architecture to predict a pseudo microstructure of the slurry. This pseudo microstructure was processed to obtain a predicted microstructure. After that, as introduced in our previous work for lithium-ion battery cathodes [28], the 3D predicted microstructure was run for a few timesteps using DEM to make the particle relaxation in the simulated slurry, which enables the final slurry microstructure to be more stable. Therefore, the proposed framework does not completely replace DEM simulations, but rather accelerates the long DEM equilibration stage by combining short DEM simulations, DL-based pseudo microstructure prediction, and a final DEM relaxation step. Model validation was performed using a dual-metric strategy, incorporating both a direct data-based comparison and an assessment derived from microstructure functional analysis. Significantly, this hybrid framework, DL-DEM, offers a major advantage by drastically reducing the computational time required for conventional DEM drying simulations without compromising the integrity of the results.

2. Methodologies

2.1. Data generation

The dataset used in this study was generated using our previously reported physics-based manufacturing modelling workflow for the fuel-electrode support [27]. This workflow employs the DEM to sequentially simulate slurry formation and subsequent drying, yielding distinct 3D mesoscale microstructures at each stage. The physicochemical properties of the casting slurry are described using a combination of Lennard-Jones FF (LJFF) [29,30] and Granular Hertz FF (GHFF) [31,32]. The LJFF approximates the nonbonded interaction between particles within the simulation box, while the GHFF governs the mechanical properties of the contacting particles. The LJFF is derived from the Lennard-Jones (LJ) potential energy expressed as

$$V(r) = 4\epsilon\left[\left(\frac{\sigma}{r}\right)^{12} - \left(\frac{\sigma}{r}\right)^{6}\right] \qquad r < r_c, \tag{1}$$

where ϵ is the potential well depth of the LJ potential curve, σ is the distance at which the inter-particle potential between the two particles is zero, r_c is the cut-off distance at which the particles stop interacting with one another, and r represents the distance between two particles measured between the centre of one particle and the centre of the other particle.

The GHFF is defined as

$$F_{GH} = \sqrt{\delta}\sqrt{\frac{R_i R_j}{R_i + R_j}}\left[\left(k_n \delta n_{ij} - m_{\text{eff}}\gamma_n \upsilon_n\right) - \left(k_t \Delta s_t + m_{\text{eff}}\gamma_t \upsilon_t\right)\right], \tag{2}$$

where R_i and R_j are the radii of two particles, δ, k_n, k_t, γ_n, γ_t, υ_n and υ_t symbolise the overlap distance, the normal elastic constant, the tangential elastic constant, viscoelastic damping constant for normal interaction, viscoelastic damping constant for tangential interaction, the relative velocity of two interacting particles in terms of normal and tangential components, respectively. Additionally, Δs_t, n_{ij}, and m_{eff} represent the tangential displacement vector between a pair of interacting particles, the unit vector along the line linking the centres of the two interacting particles, and the effective mass, $\frac{m_i m_j}{m_i + m_j}$, of both particles of mass m_i and m_j, respectively.

In the present study, we construct a dataset of slurry microstructures to train the DL model for predicting the final microstructure. Synthetic slurry microstructures for DL model training were generated via DEM simulations using the LAMMPS Molecular Dynamics Simulator [33,34], producing 3D microstructures of casting slurries with varying thicknesses and sizes. Slurry thickness was controlled by adjusting the material quantity, resulting in a higher number of particles within the simulation box. Consequently, computational time depended upon slurry volume, with larger volumes requiring longer simulation durations.

It is worth mentioning that a single formulation (52% of NiO, 35% of 8YSZ, and 13% of BDPD) and a unique FF set was employed for data generation, allowing multiple microstructures to remain physically consistent and representative of a well-defined system. This allows the dataset to capture intra-system variability arising from random particle packing, simulation box scaling, and process conditions, while maintaining a consistent physical framework for the slurry system. The approach is suitable for a proof-of-concept study aimed at validating the proposed hybrid workflow, quantifying its computational benefits, and evaluating its predictive capability.

A total of 15 simulations of solvent-based slurry were conducted on the MatriCS High Performance Computing platform at the Université de Picardie Jules Verne (Amiens, France), using one node per simulation equipped with 128 GB of RAM and 2 processors (Intel® Xeon® CPU E5-2680 v4 @2.40 GHz, 28 cores) [35]. Eight simulations were randomly used for model training and validation, while the remaining were reserved for testing. All simulations reached equilibrium after six million timesteps, with each timestep corresponding to 0.0001 microseconds. Since frames are generated every fifty thousand timesteps, each simulation produced 121 frames once the slurry microstructure equilibrated at the timesteps of 6 000 000 (Table 1). Further details on initial particle configurations, particle size distributions, and simulation parameters are available in our previous work [27]. The set of FFs used for data generation are provided in Table S1, Supporting Information.

All information about slurry microstructures generated by our DEM framework can also be found in the Supporting Information (Tables S2 and S3).

2.2. Data preprocessing

In the DEM simulation, periodic boundary conditions (PBCs) are applied in all three Cartesian directions, allowing particles to exit the simulation box on one side and re-enter from the opposite side. This presents a significant challenge for the model to learn particle behaviour near the simulation boundaries, where interactions may occur across the periodic edges. To address this limitation, unwrapped coordinates (i.e. the raw positions of particles without the effect of periodic boundary conditions, showing the continuous trajectory of a particle) were used for model training instead of wrapped coordinates. This approach enabled the model to more accurately capture particle trajectories, whereas wrapped coordinates provided only relative positions within the simulation box, making it more difficult for the DL model to learn consistent particle motions.

Moreover, from the deep-learning training perspective, in our previous study on battery electrodes, the use of wrapped coordinates under PBC produced a consistent pattern of outliers in the predicted-versus-target plots. These outliers were traced to abrupt position jumps occurring when particles crossed periodic boundaries, which introduced artificial discontinuities into the training data [36]. In a subsequent study within our group, the use of unwrapped coordinates eliminated these boundary-induced jumps and enabled smooth, continuous trajectory tracking, resulting in significantly more consistent displacement predictions across all particles [28].

Without loss of generality, relevant particle information is extracted from LAMMPS dump files, including particle types, radii, unwrapped coordinates, and coordination numbers from four earlier-stage slurry frames corresponding to timesteps 350 000, 400 000, 450 000, and 500 000. These data are then structured into a matrix format for model training.

A matrix storing the data of all particles from the ith simulation for $i = 1, \ldots, 8$ is written as

$$X_i = \begin{bmatrix} X_{i,1} \\ X_{i,2} \\ \vdots \\ X_{i,N-1} \\ X_{i,N} \end{bmatrix}, \tag{3}$$

where $X_{i,j}$ are matrices containing the jth particle information corresponding to the ith simulation for $j = 1, \ldots, N$ and expressed as

$$X_{i,j} = \begin{bmatrix} t_1^{i,j} & r_1^{i,j} & ux_1^{i,j} & uy_1^{i,j} & uz_1^{i,j} & c_1^{i,j} \\ t_2^{i,j} & r_2^{i,j} & ux_2^{i,j} & uy_2^{i,j} & uz_2^{i,j} & c_2^{i,j} \\ t_3^{i,j} & r_3^{i,j} & ux_3^{i,j} & uy_3^{i,j} & uz_3^{i,j} & c_3^{i,j} \\ t_4^{i,j} & r_4^{i,j} & ux_4^{i,j} & uy_4^{i,j} & uz_4^{i,j} & c_4^{i,j} \end{bmatrix}, \tag{4}$$

where $t_k^{i,j}$, $r_k^{i,j}$, $ux_k^{i,j}$, $uy_k^{i,j}$, $uz_k^{i,j}$, and $c_k^{i,j}$ represent the particle types, radii, unwrapped coordinates and coordination number values, respectively, corresponding to kth frame for k = 1, ⋯, 4.

Consequently, a matrix which collects the particle information from the slurry-phase simulation is expressed as follows:

$$X = \begin{bmatrix} X_1 \\ X_2 \\ X_3 \\ X_4 \\ X_5 \\ X_6 \\ X_7 \\ X_8 \end{bmatrix}. \tag{5}$$

Similarly, the output is the unwrapped coordinates of the particles, which means the particle positions without any periodic transformation in the equilibrated microstructures at timestep 6 000 000, as described earlier. These coordinates are presented as

$$Y = \begin{bmatrix} Y_1 \\ Y_2 \\ Y_3 \\ Y_4 \\ Y_5 \\ Y_6 \\ Y_7 \\ Y_8 \end{bmatrix}, \tag{6}$$

where

$$Y_i = \begin{bmatrix} Y_{i,1} \\ Y_{i,2} \\ \vdots \\ Y_{i,N-1} \\ Y_{i,N} \end{bmatrix}, \tag{7}$$

in which

$$Y_{i,1} = \begin{bmatrix} ux_{i,1} & uy_{i,1} & uz_{i,1} \\ ux_{i,2} & uy_{i,2} & uz_{i,2} \\ \vdots & \vdots & \vdots \\ ux_{i,N-1} & uy_{i,N-1} & uz_{i,N-1} \\ ux_{i,N} & uy_{i,N} & uz_{i,N} \end{bmatrix}, \tag{8}$$

where the subscripts, i and N, symbolise the ith simulation and the number of particles, respectively.

In total, the dataset consists of approximately 131 936 samples, where each sample corresponds to a particle-level representation extracted from DEM simulations. Each input sample contains a sequence of 4 timesteps with 6 particle-wise descriptors, while the corresponding output represents the unwrapped particle coordinates of the final slurry frame.

The entire dataset was randomly split into training and validation subsets containing 80% and 20% of the whole dataset, respectively. The training set was used to train the model, while the validation set was utilised to fine-tune the hyperparameters and prevent overfitting. Unseen data from new simulations was used to evaluate the model's generalisation capability.

2.3. Modified VGG16 model

VGG16, a well-known CNN architecture proposed by Karen Simonyan and Andrew Zisserman, was originally designed for image classification tasks [37]. The model typically comprises sixteen layers, including thirteen convolutional layers and three fully connected layers. In fact, the full architecture contains twenty-one layers, including the five max-pooling layers. Nevertheless, the model is referred to as VGG16 because it contains only sixteen weight layers. Although the VGG16 architecture was primarily designed for image classification, this model can be altered for regression tasks.

In this study, our particle dataset is represented as a structured matrix of particle features, exhibiting a grid-like topology suitable for 1D CNN architectures. By reshaping the original VGG16 architecture to suit a 1D regression task, we can take advantage of VGG16 spatial hierarchy to our particle dataset. Specifically, the 2D convolutional layers (Conv2D) are replaced with 1D convolutional layers (Conv1D), resulting in the internal modification of convolutional layers such as the kernel size. The pooling layer must also be adapted to maintain the consistency of the VGG16-based architecture. In particular, the max-pooling layer remains applicable, provided it operates in a manner compatible with the 1D feature sequence. Besides, the final fully connected layer is modified to perform regression instead of classification. Table 2 shows the architecture of the modified VGG16 model for regression tasks, adapted from the standard VGG16 implementation

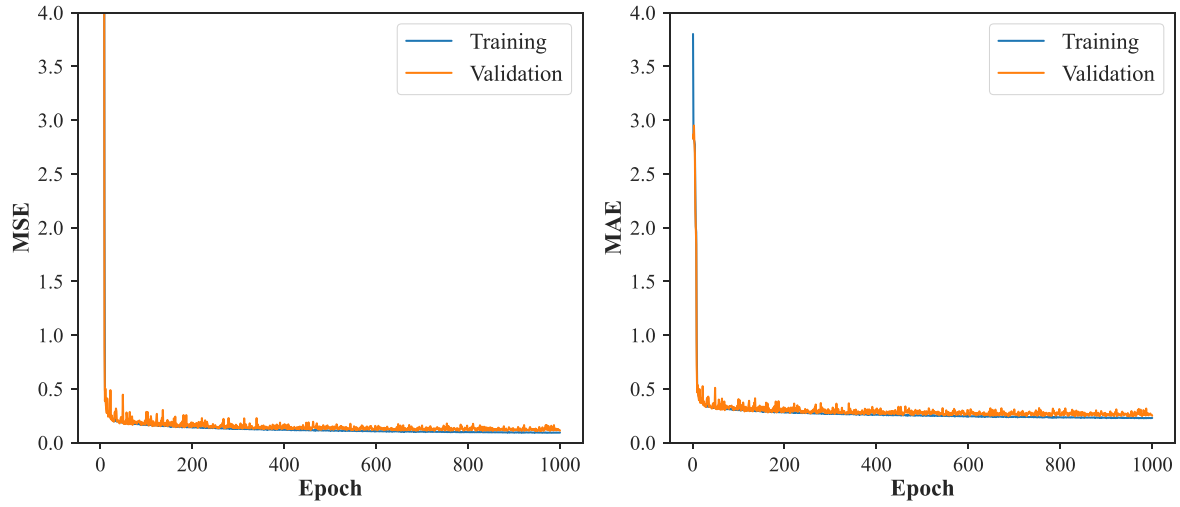

(a) *Mean squared error* (b) *Mean absolute error*

Fig. 2. (a) Mean square error and (b) Mean absolute error curves showing the evolution of training and validation performance during training of the modified VGG16 CNN. The close alignment and convergence indicate effective learning and good generalisation.

Table 2
Summary of the modified 1D VGG16 architecture for our DL model, adapted from the original 2D VGG16. The network comprises sequential convolutional blocks, followed by a flattening layer and fully connected dense layers. The final fully connected dense layer produces three regression outputs. "None" denotes a placeholder, indicating that the network can process multiple samples per gradient update.

Layer	Output shape	Parameter no.
Conv1D	(None; 4; 64)	1 216
Conv1D	(None; 4; 64)	12 352
MaxPooling1D	(None; 2; 64)	0
Conv1D	(None; 2; 128)	24 704
Conv1D	(None; 2; 128)	49 280
MaxPooling1D	(None; 1; 128)	0
Conv1D	(None; 1; 256)	98 560
Conv1D	(None; 1; 256)	196 864
Conv1D	(None; 1; 256)	196 864
MaxPooling1D	(None; 1; 256)	0
Conv1D	(None; 1; 512)	393 728
Conv1D	(None; 1; 512)	786 944
Conv1D	(None; 1; 512)	786 944
MaxPooling1D	(None; 1; 512)	0
Conv1D	(None; 1; 512)	786 944
Conv1D	(None; 1; 512)	786 944
Conv1D	(None; 1; 512)	786 944
MaxPooling1D	(None; 1; 512)	0
Flatten	(None; 512)	0
Dense	(None; 4 096)	2 101 248
Dense	(None; 4 096)	16 781 312
Dense	(None; 3)	12 291
Total		**23 803 139**

in Keras. The CNN model was implemented and trained in Python using the TensorFlow/Keras framework. The "None" in the output shape refers to a flexible batch size dimension, as per TensorFlow/Keras conventions [38,39].

The loss function and evaluation metrics used during model training to quantify the average difference between target and predicted values were the mean squared error (MSE) and mean absolute error (MAE), respectively. The loss function was used to optimise the model's hyperparameters, while the evaluation metrics were used to assess the model's performance after training. Lower MSE and MAE values demonstrate that the model's predictions are closer to the ground truth. These metrics are defined as follows:

$$\mathrm{MSE} = \frac{1}{N}\sum_{i=1}^{N}\left(\boldsymbol{Y}_i - \hat{\boldsymbol{Y}}_i\right)^2, \tag{9}$$

and

$$\mathrm{MAE} = \frac{1}{N}\sum_{i=1}^{N}\left|\boldsymbol{Y}_i - \hat{\boldsymbol{Y}}_i\right|, \tag{10}$$

where N is the number of particles, $\boldsymbol{Y}_i$ represents the unwrapped coordinates of the ith particle, and $\hat{\boldsymbol{Y}}_i$ is the predicted unwrapped coordinates of the ith particle.

To evaluate model accuracy, the coefficient of determination (R^2) was used on completely unseen dataset. This metric indicates the proportion of the total variance in the dependent variable that is explained by the model, with values closer to 1 representing better predictive performance. The coefficient of determination is defined as

$$R^2 = 1 - \frac{\sum_{i=1}^{N}\left(\boldsymbol{Y}_i - \hat{\boldsymbol{Y}}_i\right)^2}{\sum_{i=1}^{N}\left(\boldsymbol{Y}_i - \bar{\boldsymbol{Y}}\right)^2}, \tag{11}$$

where $\bar{\boldsymbol{Y}}$ is the mean of the unwrapped coordinate.

The Open Visualization Tool (OVITO) package was used for the visualisation of all 3D microstructures [40], including both target and predicted structures, for visual comparison.

2.4. Slurry microstructure post-processing framework

The proposed framework combines the DL approach already described above with DEM simulations to model the slurry microstructures. The DL model was first trained on four initial slurry-microstructure frames corresponding to the timesteps 350 000, 400 000, 450 000, and 500 000. After training, the DL model predicted the pseudo microstructure representing the slurry frame at the timestep 6 000 000, expressed in unwrapped particle coordinates. Then, this pseudo microstructure was wrapped with PBCs to obtain the predicted one using the OVITO package and used as the initial configuration for a fixed number of DEM simulation steps. These DEM simulations enable the system to relax physically, removing unphysical particle displacements which can arise from the particle wrapping process. This DEM relaxation step also helps mitigate any minor local irregularities inherited from the data-driven prediction stage. The resulting output from this procedure is a physically refined slurry microstructure (our final slurry microstructure) (Fig. 1).

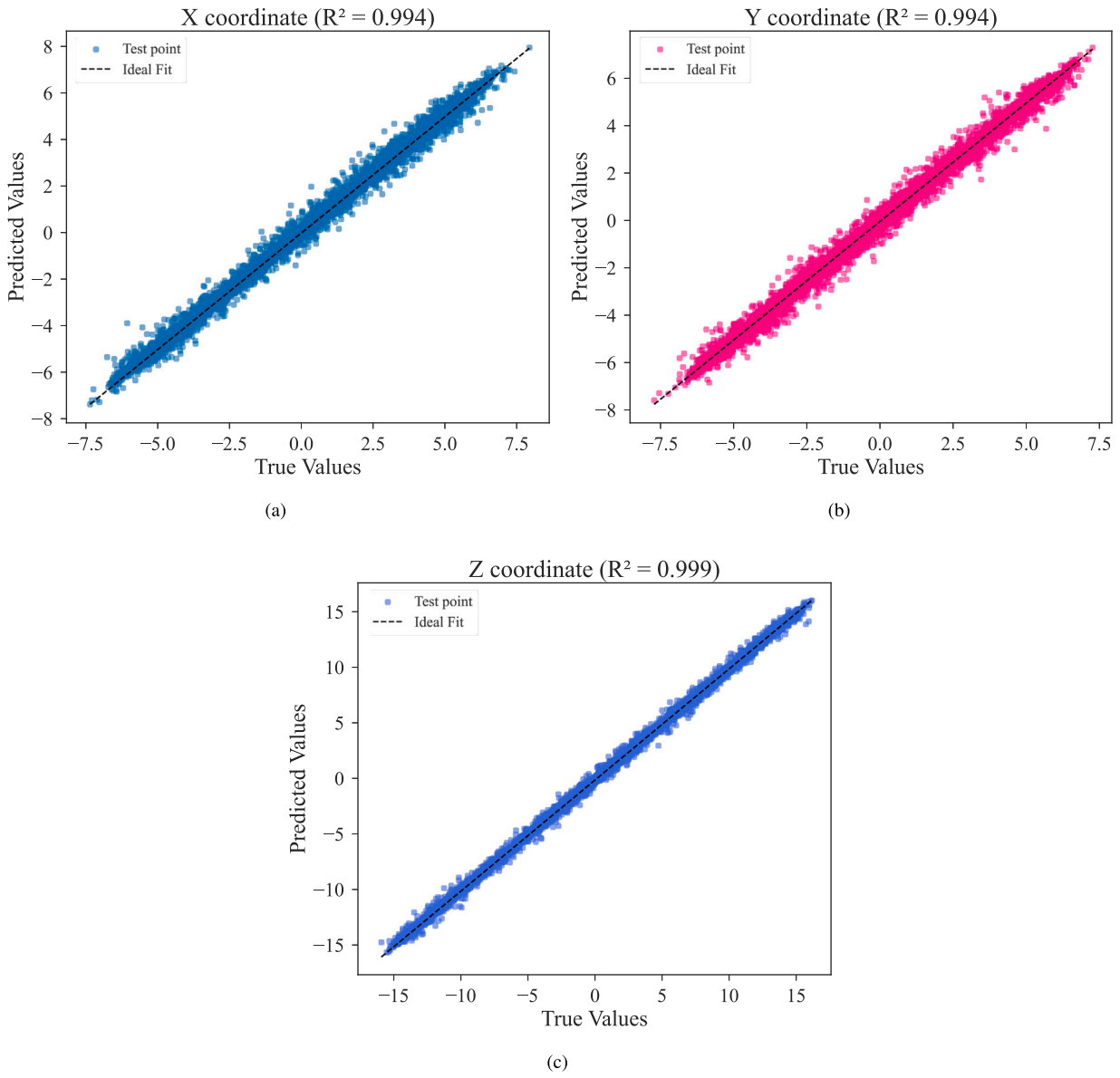

Fig. 3. Target versus predicted plot of Slurry 1 along the X, Y, and Z axes for the modified VGG16 model validating the training performance. The high R^2 scores and the close alignment between predicted and target data points around the ideal prediction line indicate extremely low error and strong agreement between predictions and ground truth.

The incorporation of DEM steps is of the utmost importance in ensuring the resulting particle configurations better reflect realistic behaviours by enforcing physical constraints to mitigate the potential unphysical jumps of particles during the PBC wrapping process. Overall, this integration of DEM into the predictive framework not only enhances the physical consistency of the slurry microstructures but also improves the reliability and accuracy of the modelling outcomes.

3. Results and discussion

3.1. Modified VGG16 performance

The modified VGG16 model was fine-tuned with different sets of hyperparameters. The best configuration was trained for 1 000 epochs with a batch size of 500, using the Adamax optimiser with a learning rate of 0.0001. Further details of the selected hyperparameters are provided in the Supporting Information (Table S4). Fig. 2 illustrates the evolution of both MSE and MAE for the training and validation sets over the epochs during the training of the modified VGG16 model. During training, both MSE (loss, Fig. 2a) and MAE (error, Fig. 2b) curves for the training and validation sets stabilised and converged, indicating that the CNN (the modified VGG16) learned effectively. The close alignment between the training and validation curves for both metrics further suggests that the model generalised well to unseen data and avoided overfitting.

The performance of the modified VGG16 model was evaluated by comparing the predicted and target values along the X, Y, and Z axes individually. Fig. 3 illustrates the predicted versus target values for each axis with respect to Slurry 1 (Table S3). In all cases, the predictions lie almost perfectly along the ideal prediction line, suggesting extremely low error across all spatial directions. Furthermore, for each axis, the coefficient of determination R^2 was calculated to quantify how well the model predictions matched the ground truth. The resulting R^2 values were 0.994 for X, 0.994 for Y, and 0.999 for Z, indicating a very strong correlation between predicted and true values with an average R^2 of 0.996 for an unseen slurry dataset. The slightly improved predictive performance in the z-coordinate may be related to the structural evolution of the slurry system under the NPT ensemble conditions used

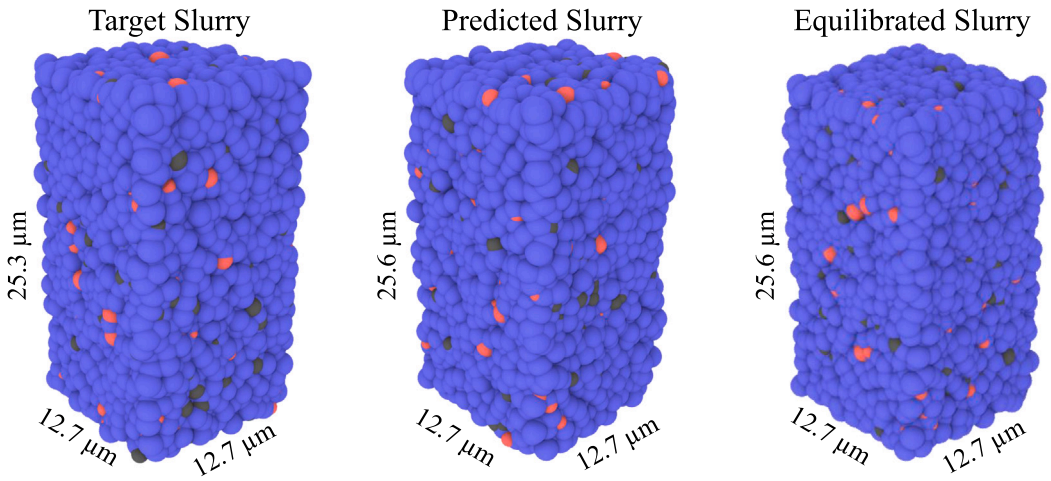

Fig. 4. Unseen Slurry microstructure along with thickness comparison for the case of Slurry 2 (Table S3).

in the present simulations. During equilibration, positional changes in the x- and y-directions may remain comparatively small, whereas relatively larger structural changes may occur along the z-direction, which corresponds to the slurry thickness direction. As a result, the z-coordinate may contain a clearer temporal trend that the CNN model can learn more readily. In contrast, the smaller variations in x and y may be more influenced by local fluctuations, leading to slightly larger scatter in the corresponding predictions shown in Figs. 3 and later in Fig. 5.

These results demonstrate that the model not only predicts the overall trend of the data but also maintains high accuracy at the individual-axis level, providing confidence in its generalisation capability. The high R^2 values and the close alignment of predictions with target values indicate robust performance of the model in reconstructing multi-dimensional outputs.

3.2. Microstructure analysis for comparing hybrid approach

3.2.1. Visual comparisons

A visual comparison of the slurry microstructures was performed using OVITO. The target microstructure was generated directly using the physics-based simulation approach, while the predicted microstructure was obtained using the modified VGG16 model. To obtain the equilibrated microstructure, the predicted microstructure was fed back into the DEM simulation framework to undergo an equilibration step, in an approach proposed in our previous work [28,36,41], here referred to equilibrated microstructure (Fig. 4). This step is crucial, as it uses the strengths of the physics-based model to refine and stabilise the structure. The computational cost of the hybrid workflow is dominated by the DEM relaxation step, whereas the CNN model adds only negligible additional runtimer. Consequently, the total wall time of our hybrid framework is approximately 30 min, depending upon the simulated slurry volume. In contrast, the full DEM simulation requires approximately 20.5 h, demonstrating a substantial overall acceleration. As shown in Figs. 4, the three microstructures appear visually different, which is expected because the applied DL approach is data-driven. Therefore, measurements of density and volume were performed to compare the microstructures. As can be observed in Table 3, for microstructures 2 and 3, the DL-DEM model closely matches DEM predictions, indicating strong baseline predictive accuracy.

As microstructural thickness increases, the hybrid model adapts its predictions but begins to show noticeable deviations, particularly in Microstructure 6, where the density prediction increases to 2.7822 g/cm^3 compared to the DEM estimate of 2.2437 g/cm^3. These deviations can be attributed to the random fitting of particles during simulation, which introduces natural variation in particle counts, size distributions, and packing arrangements across microstructures. Such variability becomes more pronounced in larger and more complex systems, leading to higher prediction differences. For instance, in Microstructure 6, the hybrid model deviated by approximately 23.6% compared to other microstructures within the same complexity regime.

Table 3
Comparison of density and volume for different unseen slurry microstructures.

Slurry ID	Model	Density $[g/cm^3]$	Volume $[\mu m^3]$
2	DEM	2.2430	4 081
	DL-DEM	2.2169	4 129
3	DEM	2.2415	4 091
	DL-DEM	2.2486	4 078
4	DEM	2.2422	8 096
	DL-DEM	2.3810	7 624
5	DEM	2.2419	8 126
	DL-DEM	2.3870	7 632
6	DEM	2.2437	20 390
	DL-DEM	2.7822	16 443
7	DEM	2.2406	16 360
	DL-DEM	2.2799	16 087

Despite these differences, the overall performance of the DL-DEM framework remains robust. Across all microstructures, the mean absolute difference in density was approximately 0.15 g/cm^3, with a maximum deviation of 0.54 g/cm^3 observed in the most complex case. Volume predictions followed similar trends, remaining within physically plausible ranges and reflecting changes in microstructural complexity. This stability indicates that the modified VGG16-based hybrid model demonstrates good generalisability across diverse microstructures without the need for modifying the neural network architecture further. The visual comparisons for all other test slurries can be found in Figure S1 in the Supporting Information.

3.2.2. Data metrics and physics-based analysis

Data metrics. To evaluate the predictive performance of the proposed hybrid DL-DEM model, standard regression metrics were calculated by comparing the predicted and target particle coordinates for each unseen slurry microstructure (Table 4). These metrics include the MSE and MAE, which quantify the magnitude of positional differences, and the R^2, which assesses how well the predicted data captures the variability present in the target data.

Across all microstructures, the results show consistently low error values, with MSE ranging from 0.060 to 0.199 and MAE from 0.165 to 0.348. The lowest errors were observed for Slurry 2 and Slurry 3 (MSE = 0.060–0.068; MAE = 0.165–0.178), while slightly higher values

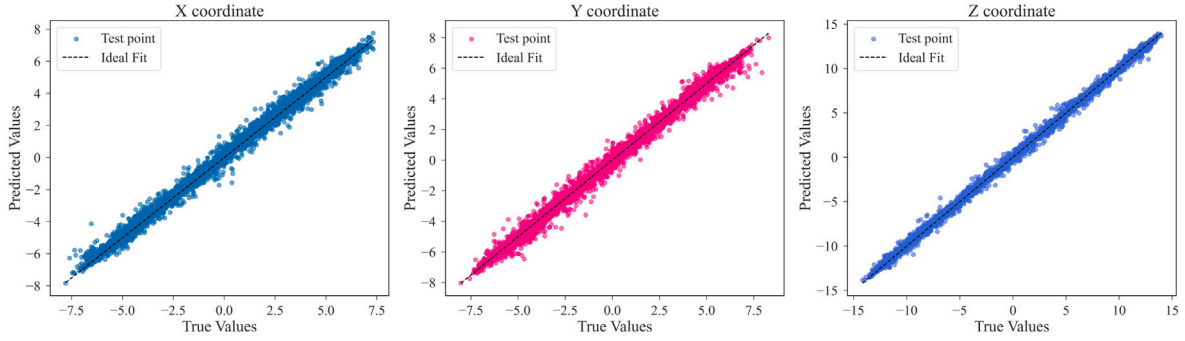

(a) *Slurry 2*

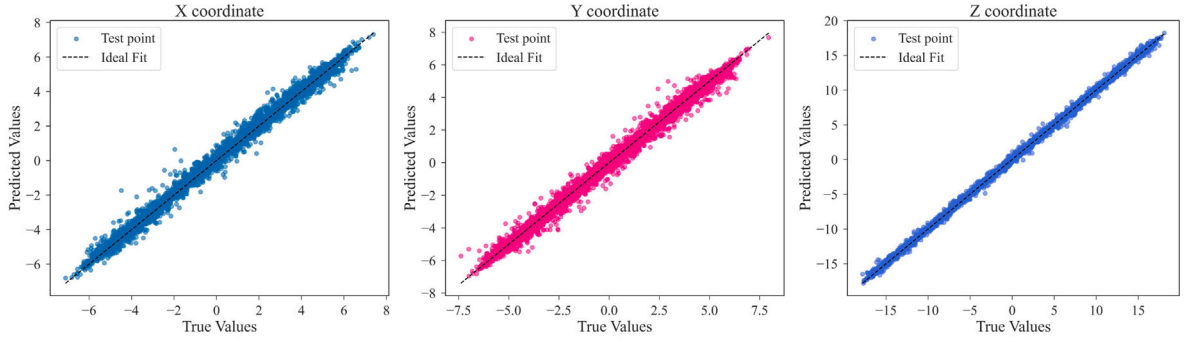

(b) *Slurry 3*

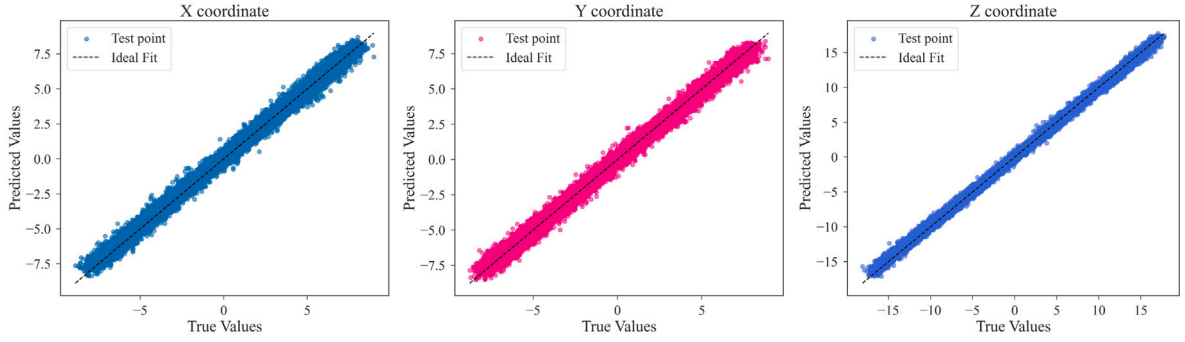

(c) *Slurry 4*

Fig. 5. Target vs. predicted plot across different unseen slurry microstructures: (a) Slurry 2, (b) Slurry 3, (c) Slurry 4, (d) Slurry 5, (e) Slurry 6, and (f) Slurry 7 along the X, Y, and Z axes, where the ideal fit represents a perfect correlation between predicted and true values (particle coordinates).

Table 4
Performance metrics (MSE, MAE, and R^2) for the hybrid DL-DEM model across unseen slurry microstructures.

Slurry ID	MSE Target vs Predicted	MAE Target vs Predicted	R^2 Target vs Predicted
2	0.068	0.178	0.996
3	0.060	0.165	0.996
4	0.165	0.316	0.995
5	0.152	0.305	0.995
6	0.199	0.348	0.996
7	0.094	0.226	0.998

were noted for Slurries 4–6. These low errors indicate that the predicted particle positions are very close to the target positions. Furthermore, the R^2 values remain exceptionally high (0.995–0.998) across all cases, demonstrating that the hybrid model effectively preserves the variability and overall distribution of the target coordinates.

In addition to the quantitative metrics, the predicted particle coordinates were plotted against the target coordinates for all axes (X, Y, and Z) across each microstructure (Fig. 5). The scatter plots demonstrate that the predicted points lie very close to the best-fitting line, indicating excellent agreement between the predicted and target coordinates. This visual confirmation supports the earlier data metric analysis, showing that the model accurately predicts particle positions across all spatial dimensions and for all microstructures. While this demonstrates numerical accuracy, the structural fidelity of the predicted microstructures will be further assessed using RDF analysis in the following section.

Radial distribution analysis. While the correlation plot (Fig. 5) confirmed good agreement between predicted and target microstructural coordinates, the RDF was computed for both the equilibrated and the physics-based microstructures. The RDF was calculated separately for each particle type combination (BDPD-NiO-8YSZ and NiO-8YSZ). Because the spatial scales and interaction ranges vary between these combinations, the bin size/histogram resolution (Δr) and maximum cutoff distance (r_{max}) were adjusted to accurately capture both local

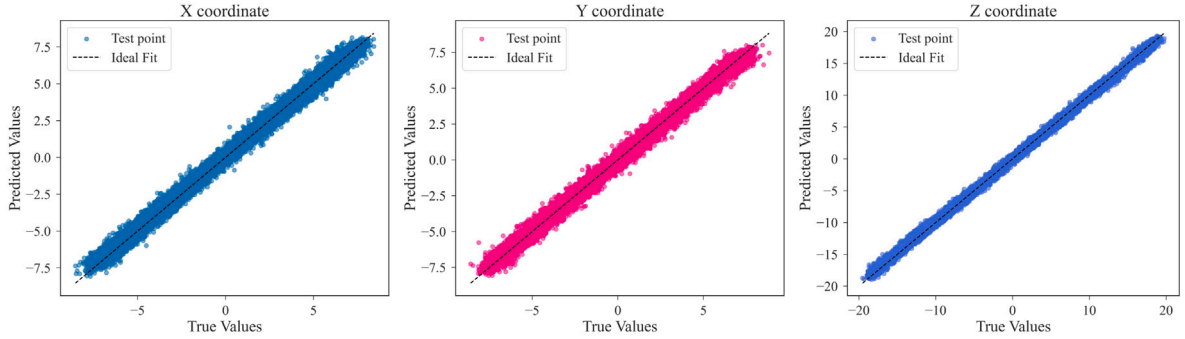

(d) *Slurry 5*

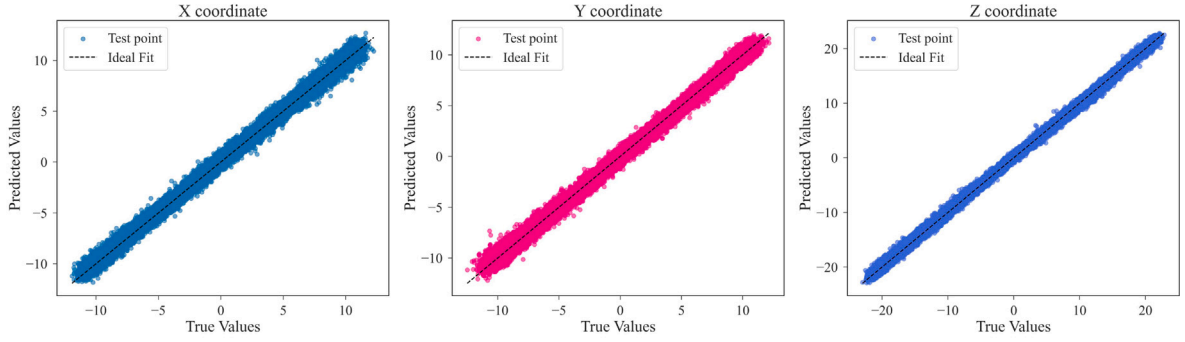

(e) *Slurry 6*

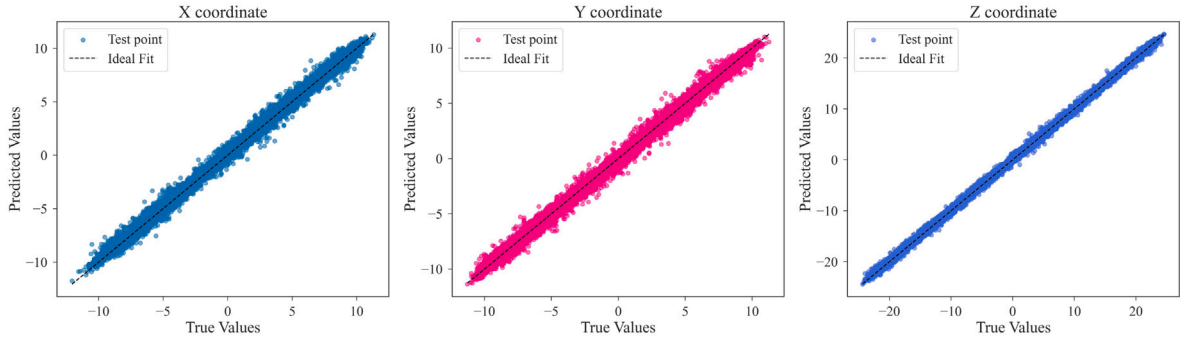

(f) *Slurry 7*

Fig. 5. (*continued*).

and medium-range structural features. The respective RDF curves and specific parameters used are provided in the caption of Fig. 6.

Regarding the RDF of all particle pairs (BDPD-NiO-8YSZ), (Figs. 6a, 6c, 6e, 6g, 6i, and 6k), it can be observed that the equilibrated microstructure shows peaks for the first and subsequent nearest neighbours that align very well with the target in the cases of slurries 2, 3, 4, 5, and 7, suggesting that the hybrid approach (DL-DEM) accurately reproduces the local structural arrangement of these microstructures. Specifically, the first peaks of the target and equilibrated slurries were slightly different at short-range order distances (r = 0.8 μm). The second peak at r = 1.1 μm appears at nearly identical positions. The identical alignment was also observed at medium-range and long-range order (r > 2 μm). This implies that despite the bias at the short-range order, the hybrid model successfully captures the fundamental state of the slurry. However, in the case of slurry 6, the RDF of the equilibrated microstructure follows the same overall trend but is slightly left-shifted, indicating that the average interparticle distances are smaller, which may be due to higher local packing density or differences in particle interactions for this formulation.

Since BDPD is present in abundance, it can significantly influence the overall microstructure. To isolate the effect of the remaining components, the RDF of NiO-8YSZ was also compared separately (Figs. 6b, 6d, 6f, 6h, 6j, and 6l). A similar trend was observed across slurries 2, 3, 4, 5, and 7. The hybrid model has difficulty accurately predicting the peak at short-range order (r = 0.3–0.9 μm). The correlation between RDFs of target and equilibrated slurries was nearly identical at longer-range distances (r > 2 μm), where the peaks of the equilibrated microstructure align well with the target. However, in the case of slurry 6, although the overall trend is maintained, the peak of the equilibrated microstructure is lower than that of the target, indicating a slightly reduced local ordering or weaker correlations between NiO and 8YSZ particles in this formulation.

Overall, the RDF analysis demonstrates that the predicted microstructures obtained using the hybrid approach (DL-DEM) reliably reproduce the local and intermediate structural arrangements of the target microstructures across most slurries. The close alignment of peaks for both BDPD-NiO-8YSZ and NiO-8YSZ, except for minor deviations in slurry 6, confirms the accuracy and robustness of the hybrid method in capturing realistic particle distributions and correlations.

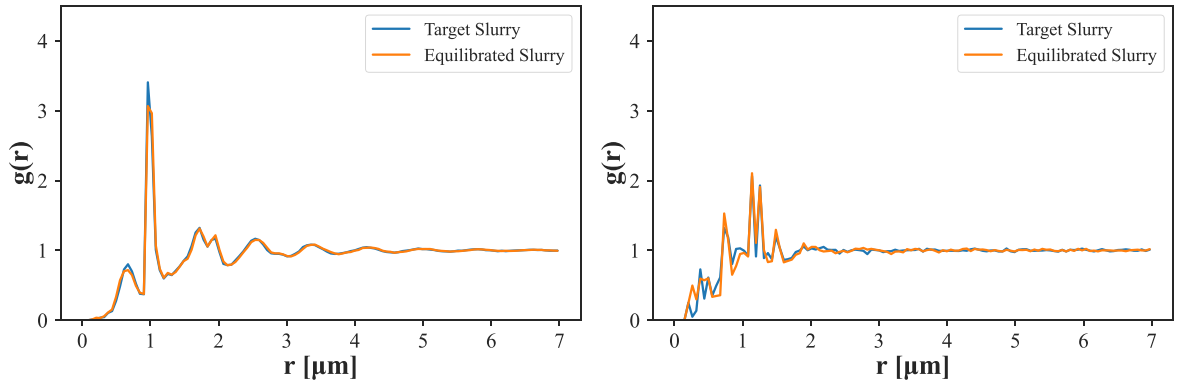

(a) *Slurry 2: All particle pairs*

(b) *Slurry 2: NiO-8YSZ*

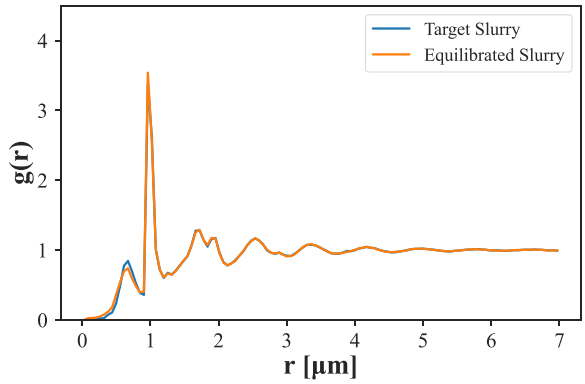

(c) *Slurry 3: All particle pairs*

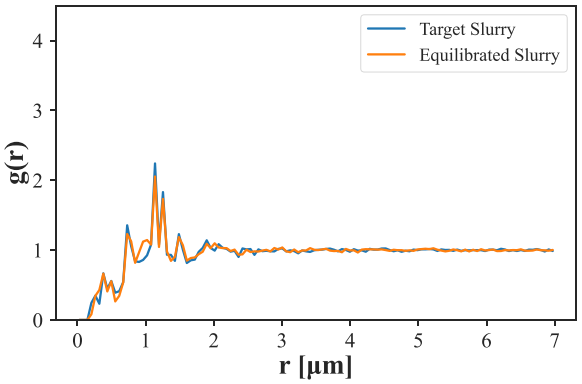

(d) *Slurry 3: NiO-8YSZ*

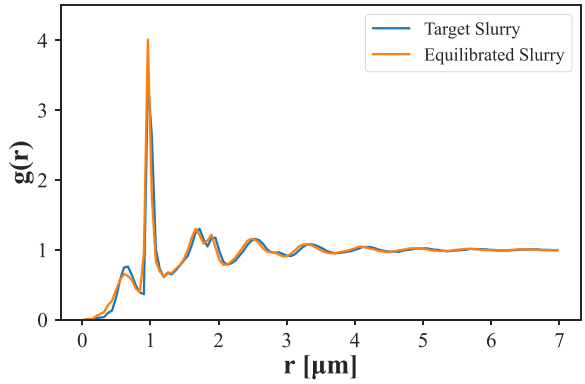

(e) *Slurry 4: All particle pairs*

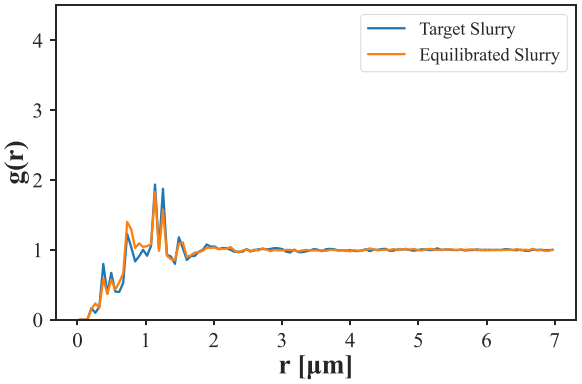

(f) *Slurry 4: NiO-8YSZ*

Fig. 6. Pair-wise RDFs comparing target and equilibrated microstructures of the unseen slurry microstructures: (a) Slurry 2: All particle pairs, (b) Slurry 2: NiO-8YSZ, (c) Slurry 3: All particle pairs, (d) Slurry 3: NiO-8YSZ, (e) Slurry 4: All particle pairs, (f) Slurry 4: NiO-8YSZ, (g) Slurry 5: All particle pairs, (h) Slurry 5: NiO-8YSZ, (i) Slurry 6: All particle pairs, (j) Slurry 6: NiO-8YSZ, (k) Slurry 7: All particle pairs, and (l) Slurry 7: NiO-8YSZ. The cutoff radius used for the RDF calculation is $r_c = 7$ µm, and the histogram resolution is $\Delta r = 0.0583$, corresponding to 120 bins.

4. Conclusions and perspectives

In this study, we introduced a hybrid surrogate modelling framework that integrates DL with physics-based DEM simulations to overcome the high computational cost typically associated with repeated DEM runs and FF fitting for the SOC substrate microstructure generation. By training the modified VGG16 network on microstructural data from DEM simulations of the slurry preparation for tape casting, the proposed hybrid model could predict final slurry microstructures efficiently. These predictions were subsequently equilibrated using DEM to ensure physical realism, creating a framework that leverages the strengths of both data-driven and physics-based approaches.

The hybrid approach demonstrated strong predictive accuracy across multiple slurry microstructures, as confirmed by low error metrics and RDF analyses. Overall, the framework reliably captures local and intermediate structural arrangements. This methodology significantly accelerates validation and optimisation tasks that would otherwise rely solely on computationally intensive DEM simulations.

The present study is restricted to a single slurry formulation and a single set of force field parameters as a proof-of-concept investigation for SOC fuel-electrode substrates. However, in one of our previous studies in the context of battery electrodes, we demonstrated that, owing to the similarity in simulation configuration, the trained neural network can be readily adapted to new slurry formulations or different

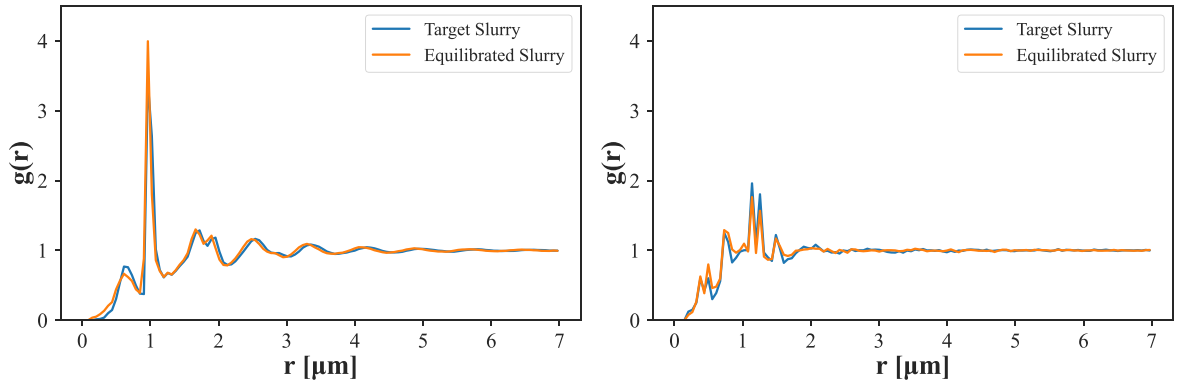

(g) *Slurry 5: All particle pairs*

(h) *Slurry 5: NiO-8YSZ*

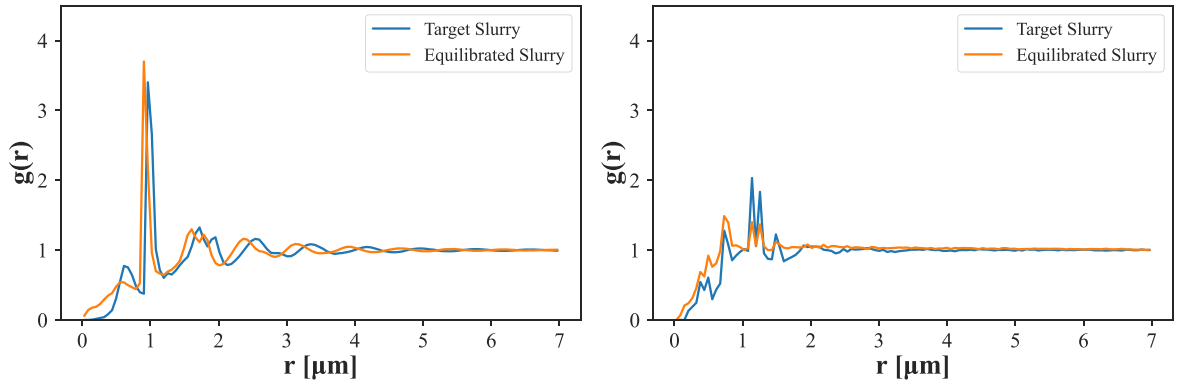

(i) *Slurry 6: All particle pairs*

(j) *Slurry 6: NiO-8YSZ*

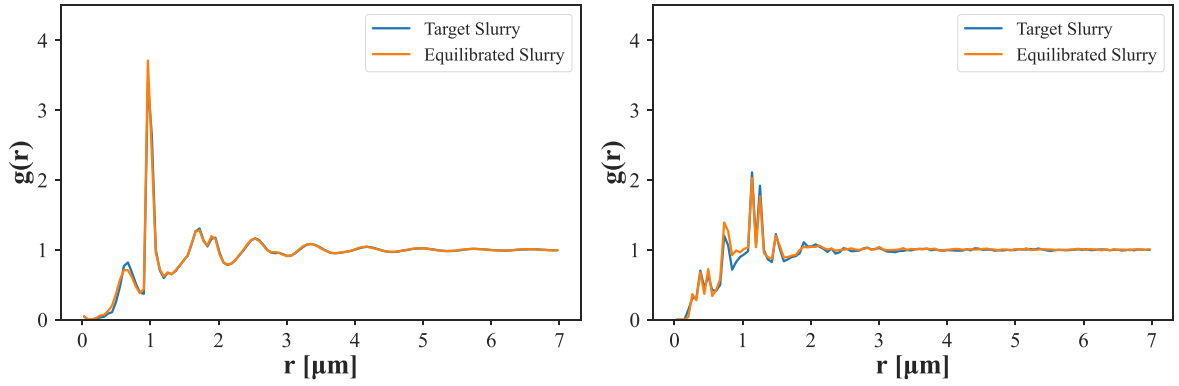

(k) *Slurry 7: All particle pairs*

(l) *Slurry 7: NiO-8YSZ*

Fig. 6. (*continued*).

force-field parameter sets with only minimal fine-tuning or retraining. The same rationale is expected to apply to the VGG16 model used in the present work, as it is developed within the same simulation framework and configuration under the ARTISTIC framework for battery manufacturing.

Our hybrid surrogate approach can be further developed to enhance both accuracy and generality using various formulations and corresponding calibrated FFs, which was not considered in this first hybrid modelling proof of concept. Furthermore, this framework can be extended to predict dried substrate microstructures associated with the drying process of tape casting and can even be adapted to model the manufacturing processes of other SOC functional layers. Moreover, given the inherent stochasticity in slurry particle packing, future work should also explore probabilistic surrogate strategies, such as conditional variational autoencoders, to quantify predictive confidence and better represent the natural variability of the packing process [28]. By bridging experimental data, physics-based simulations, and data-driven methods, the hybrid approach provides a scalable and efficient strategy for modelling SOC slurry processing, representing a step forward toward practical, high-throughput, and experimentally validated digital models for future research in tape casting of ceramic components.

CRediT authorship contribution statement

Tan Le-Dinh: Writing – original draft, Visualization, Validation, Software, Methodology, Investigation, Formal analysis, Data curation, Conceptualization. **Utkarsh Vijay:** Writing – review & editing, Validation, Formal analysis, Conceptualization. **Diego E. Galvez-Aranda:**

Writing – review & editing, Validation, Software, Methodology, Conceptualization. **Hartmut Schlenz:** Writing – review & editing, Supervision. **Norbert H. Menzler:** Writing – review & editing, Supervision. **Olivier Guillon:** Funding acquisition. **Alejandro A. Franco:** Writing – review & editing, Supervision, Resources, Project administration, Methodology, Funding acquisition, Conceptualization.

Declaration of competing interest

The authors declare that they have no known competing financial interests or personal relationships that could have appeared to influence the work reported in this paper.

Acknowledgements

T.L.D and A.A.F acknowledge the Region Hauts-de-France and Université de Picardie Jules Verne for the funding support. U.V. and A.A.F. acknowledge funding from the European Union's Horizon 2020 reasearch and innovation program under the Marie Schlodowska-Curie Action COFUND - Grant Agreement No: 945357. A.A.F. and D. E. G. acknowledge the European Research Council for the funding support through the ERC Proof-of-Concept Grant No. 101069244 (SMARTISTIC project). A.A.F. and D. E. G. acknowledge the funding support of the French National Research Agency under the France 2030 program (Grant ANR-22-PEBA-0002, PEPR project "BATMAN"). T.L.D., H.S., N.H.M., O.G. and A.A.F. gratefully acknowledge funding by the Federal Ministry of Economic Affairs and Energy of Germany (Bundesministerium für Wirtschaft und Energie, Project-No.: 03EI3085 A, ML4SOC). A.A.F. acknowledges the Institut Universitaire de France for the support. T.L.D, H.S., N.H.M., and O.G. acknowledge Forschungzentrum Jülich GmbH for the support. The authors acknowledge Dr. Francisco Fernandez, postdoctoral researcher at LRCS, for the proofreading of the article and useful comments.

Appendix A. Supplementary data

Supplementary material related to this article can be found online at https://doi.org/10.1016/j.jpowsour.2026.240447.

Data availability

Data will be made available on request.

References

[1] S. Sarner, A. Schreiber, N.H. Menzler, O. Guillon, Recycling strategies for solid oxide cells, Adv. Energy Mater. 12 (35) (2022) 2201805, http://dx.doi.org/10.1002/aenm.202201805.

[2] C. Lenser, D. Udomsilp, N.H. Menzler, P. Holtappels, T. Fujisaki, L. Kwati, H. Matsumoto, A.G. Sabato, F. Smeacetto, A. Chrysanthou, S. Molin, 9 - solid oxide fuel and electrolysis cells, in: O. Guillon (Ed.), Advanced Ceramics for Energy Conversion and Storage, in: Elsevier Series on Advanced Ceramic Materials, Elsevier, 2020, pp. 387–547, http://dx.doi.org/10.1016/B978-0-08-102726-4.00009-0.

[3] S. He, Y. Zou, K. Chen, S.P. Jiang, C.P.S. Jiang, A critical review of key materials and issues in solid oxide cells, Interdiscip. Mater. 2 (2023) 111–136, http://dx.doi.org/10.1002/IDM2.12068.

[4] F. Tietz, H.P. Buchkremer, D. Stöver, Components manufacturing for solid oxide fuel cells, Solid State Ion. 152–153 (2002) 373–381, http://dx.doi.org/10.1016/S0167-2738(02)00344-2.

[5] E.R.T. Richard E. Mistler, Tape Casting: theory and Practice, The American Ceramic Society, Westerville, OH, 2000.

[6] C. Pagnoux, T. Chartier, M. de F. Granja, F. Doreau, J. Ferreira, J. Baumard, Aqueous suspensions for tape-casting based on acrylic binders, J. Eur. Ceram. Soc. 18 (3) (1998) 241–247, http://dx.doi.org/10.1016/S0955-2219(97)00115-5.

[7] N. Menzler, F. Tietz, S. Uhlenbruck, H. Buchkremer, D. Stöver, Materials and manufacturing technologies for solid oxide fuel cells, J. Mater. Sci. 45 (2010) 3109–3135, http://dx.doi.org/10.1007/s10853-010-4279-9.

[8] P. Vozdecky, A. Roosen, Q. Ma, F. Tietz, H. Buchkremer, Properties of tape-cast Y-substituted strontium titanate for planar anode substrates in SOFC applications, J. Mater. Sci. 46 (2011) 3493–3499, http://dx.doi.org/10.1007/s10853-011-5255-8.

[9] D. Gardini, M. Deluca, M. Nagliati, C. Galassi, Flow properties of PLZTN aqueous suspensions for tape casting, Ceram. Int. 36 (2010) 1687–1696, http://dx.doi.org/10.1016/J.CERAMINT.2010.03.011.

[10] J.H. Kim, H. Ko, D.H. Yeo, Z. Park, U. Kumar, K.H. Yoo, A. Nasridinov, S.B. Cho, A versatile strategy for hybridizing small experimental and large simulation data: A case for ceramic tape-casting process, Mater. Des. 234 (2023) http://dx.doi.org/10.1016/j.matdes.2023.112357.

[11] M. Jabbari, R. Bulatova, A.I. Tok, C.R. Bahl, E. Mitsoulis, J.H. Hattel, Ceramic tape casting: A review of current methods and trends with emphasis on rheological behaviour and flow analysis, Mater. Sci. Eng.: B 212 (2016) 39–61, http://dx.doi.org/10.1016/J.MSEB.2016.07.011.

[12] M. Descamps, G. Ringuet, D. Leger, B. Thierry, Tape-casting: Relationship between organic constituents and the physical and mechanical properties of tapes, J. Eur. Ceram. Soc. 15 (1995) 357–362, http://dx.doi.org/10.1016/0955-2219(95)90360-U.

[13] ERC Artistic. https://www.erc-artistic.eu/. (Accessed 30 April 2025).

[14] T. Lombardo, J.B. Hoock, E.N. Primo, A.C. Ngandjong, M. Duquesnoy, A.A. Franco, Accelerated optimization methods for force-field parametrization in battery electrode manufacturing modeling, Batter. Supercaps 3 (2020) 721–730, http://dx.doi.org/10.1002/BATT.202000049.

[15] T. Lombardo, A.C. Ngandjong, A. Belhcen, A.A. Franco, Carbon-binder migration: A three-dimensional drying model for lithium-ion battery electrodes, Energy Storage Mater. 43 (2021) 337–347, http://dx.doi.org/10.1016/J.ENSM.2021.09.015.

[16] A.C. Ngandjong, T. Lombardo, E.N. Primo, M. Chouchane, A. Shodiev, O. Arcelus, A.A. Franco, Investigating electrode calendering and its impact on electrochemical performance by means of a new discrete element method model: Towards a digital twin of li-ion battery manufacturing, J. Power Sources 485 (2021) 229320, http://dx.doi.org/10.1016/J.JPOWSOUR.2020.229320.

[17] T. Lombardo, F. Caro, A.C. Ngandjong, J.B. Hoock, M. Duquesnoy, J.C. Delepine, A. Ponchelet, S. Doison, A.A. Franco, The ARTISTIC online calculator: Exploring the impact of lithium-ion battery electrode manufacturing parameters interactively through your browser, Batter. Supercaps 5 (2022) e202100324, http://dx.doi.org/10.1002/BATT.202100324.

[18] F.M. Zanotto, D.Z. Dominguez, E. Ayerbe, I. Boyano, C. Burmeister, M. Duquesnoy, M. Eisentraeger, J.F. Montaño, A. Gallo-Bueno, L. Gold, F. Hall, N. Kaden, B. Muerkens, L. Otaegui, Y. Reynier, S. Stier, M. Thomitzek, A. Turetskyy, N. Vallin, J. Wessel, X. Xu, J. Abbasov, A.A. Franco, Data specifications for battery manufacturing digitalization: Current status, challenges, and opportunities, Batter. Supercaps 5 (2022) e202200224, http://dx.doi.org/10.1002/BATT.202200224.

[19] J.F. Troncoso, F.M. Zanotto, D.E. Galvez-Aranda, D.Z. Dominguez, L. Denisart, A.A. Franco, The ARTISTIC battery manufacturing digitalization initiative: From fundamental research to industrialization, Batter. Supercaps 8 (2025) e202400385, http://dx.doi.org/10.1002/BATT.202400385.

[20] W. Schafbauer, N.H. Menzler, H.P. Buchkremer, Tape casting of anode supports for solid oxide fuel cells at forschungszentrum Jülich, Int. J. Appl. Ceram. Technol. 11 (2014) 125–135, http://dx.doi.org/10.1111/J.1744-7402.2012.02839.X.

[21] A. Krizhevsky, I. Sutskever, G.E. Hinton, ImageNet classification with deep convolutional neural networks, in: F. Pereira, C. Burges, L. Bottou, K. Weinberger (Eds.), in: Advances in Neural Information Processing Systems, vol. 25, Curran Associates, Inc., 2012.

[22] C. Szegedy, W. Liu, Y. Jia, P. Sermanet, S. Reed, D. Anguelov, D. Erhan, V. Vanhoucke, A. Rabinovich, Going deeper with convolutions, in: 2015 IEEE Conference on Computer Vision and Pattern Recognition, CVPR, 2015, pp. 1–9, http://dx.doi.org/10.1109/CVPR.2015.7298594.

[23] R. Girshick, J. Donahue, T. Darrell, J. Malik, Rich feature hierarchies for accurate object detection and semantic segmentation, Proc. IEEE Comput. Soc. Conf. Comput. Vis. Pattern Recognit. (2013) 580–587, http://dx.doi.org/10.1109/CVPR.2014.81.

[24] P. Sermanet, D. Eigen, X. Zhang, M. Mathieu, R. Fergus, Y. LeCun, OverFeat: Integrated recognition, localization and detection using convolutional networks, in: 2nd International Conference on Learning Representations, ICLR 2014 - Conference Track Proceedings, International Conference on Learning Representations, ICLR, 2013.

[25] F. Sultana, A. Sufian, P. Dutta, Evolution of image segmentation using deep convolutional neural network: A survey, Knowl.-Based Syst. 201–202 (2020) 106062, http://dx.doi.org/10.1016/j.knosys.2020.106062.

[26] S. Lathuilière, P. Mesejo, X. Alameda-Pineda, R. Horaud, A comprehensive analysis of deep regression, IEEE Trans. Pattern Anal. Mach. Intell. 42 (9) (2020) 2065–2081, http://dx.doi.org/10.1109/TPAMI.2019.2910523.

[27] T. Le-Dinh, M. Alabdali, F.M. Zanotto, H. Schlenz, N.H. Menzler, O. Guillon, A.A. Franco, Coarse-grained physics-based modelling for tape casting of fuel-electrode supports in solid oxide cells, J. Power Sources 662 (2026) 238655, http://dx.doi.org/10.1016/j.jpowsour.2025.238655.

[28] U. Vijay, F. Fernandez, S.B.H. Ali, M. Asch, A.A. Franco, Surrogate modeling of lithium-ion battery electrode manufacturing by combining physics-based simulation and deep learning, Batter. Supercaps (2025) e202500433, http://dx.doi.org/10.1002/BATT.202500433.

[29] J.E. Lennard-Jones, Cohesion, Proc. Phys. Soc. 43 (5) (1931) 461, http://dx.doi.org/10.1088/0959-5309/43/5/301.

[30] pair_style lj/cut command — LAMMPS documentation. https://docs.lammps.org/pair_lj.html. (Accessed 30 April 2025).

[31] K. Johnson, K. Kendall, A. Roberts, Surface energy and contact of elastic solids, Proc. R. Soc. A: Math. Phys. Eng. Sci. 324 (1971) 301–313, http://dx.doi.org/10.1098/rspa.1971.0141.

[32] pair_style granular command — LAMMPS documentation. https://docs.lammps.org/pair_gran.html. (Accessed 30 April 2025).

[33] LAMMPS molecular dynamics simulator, 2025, https://www.lammps.org/#gsc.tab=0. (Accessed 30 April 2025).

[34] A.P. Thompson, H.M. Aktulga, R. Berger, D.S. Bolintineanu, W.M. Brown, P.S. Crozier, P.J. in 't Veld, A. Kohlmeyer, S.G. Moore, T.D. Nguyen, R. Shan, M.J. Stevens, J. Tranchida, C. Trott, S.J. Plimpton, LAMMPS - a flexible simulation tool for particle-based materials modeling at the atomic, meso, and continuum scales, Comp. Phys. Comm. 271 (2022) 108171, http://dx.doi.org/10.1016/j.cpc.2021.108171.

[35] MatriCS plateform, 2025, https://www.matrics.u-picardie.fr/en/documentation-2/partitions/. (Accessed 22 July 2025).

[36] U. Vijay, D.E. Galvez-Aranda, F.M. Zanotto, T. Le-Dinh, M. Alabdali, M. Asch, A.A. Franco, A hybrid modelling approach coupling physics-based simulation and deep learning for battery electrode manufacturing simulations, Energy Storage Mater. 75 (2025) 103883, http://dx.doi.org/10.1016/J.ENSM.2024.103883.

[37] K. Simonyan, A. Zisserman, Very deep convolutional networks for large-scale image recognition, in: 3rd International Conference on Learning Representations, ICLR 2015 - Conference Track Proceedings, International Conference on Learning Representations, ICLR, 2014.

[38] M. Abadi, A. Agarwal, P. Barham, E. Brevdo, Z. Chen, C. Citro, G.S. Corrado, A. Davis, J. Dean, M. Devin, S. Ghemawat, I. Goodfellow, A. Harp, G. Irving, M. Isard, Y. Jia, R. Jozefowicz, L. Kaiser, M. Kudlur, J. Levenberg, D. Mané, R. Monga, S. Moore, D. Murray, C. Olah, M. Schuster, J. Shlens, B. Steiner, I. Sutskever, K. Talwar, P. Tucker, V. Vanhoucke, V. Vasudevan, F. Viégas, O. Vinyals, P. Warden, M. Wattenberg, M. Wicke, Y. Yu, X. Zheng, TensorFlow: Large-Scale Machine Learning on Heterogeneous Systems, 2015, Software available from tensorflow.org.

[39] F. Chollet, et al., Keras, 2015, https://keras.io.

[40] A. Stukowski, Visualization and analysis of atomistic simulation data with OVITO–the open visualization tool, Modelling Simul. Mater. Sci. Eng. 18 (1) (2009) 015012, http://dx.doi.org/10.1088/0965-0393/18/1/015012.

[41] D.E. Galvez-Aranda, F. Fernandez, A.A. Franco, Physics-assisted machine learning for the simulation of the slurry drying in the manufacturing process of battery electrodes: A hybrid time-dependent VGG16-DEM model, ACS Appl. Mater. Interfaces 17 (2025) 32150–32162, http://dx.doi.org/10.1021/ACSAMI.4C23103.